frontiers | Frontiers in Space Technologies

TYPE Original Research
PUBLISHED 01 March 2024
DOI 10.3389/frspt.2024.1336548

OPEN ACCESS

EDITED BY
Marek Tulej,
University of Bern, Switzerland

REVIEWED BY
Rico Georgio Fausch,
University Hospital of Bern, Switzerland
Pavel Pořízka,
Brno University of Technology, Czechia

*CORRESPONDENCE
Kristin Rammelkamp,
kristin.rammelkamp@dlr.de
Susanne Schröder,
susanne.schroeder@dlr.de

RECEIVED 10 November 2023
ACCEPTED 19 February 2024
PUBLISHED 01 March 2024

CITATION
Rammelkamp K, Schröder S, Lomax BA, Clavé E and Hübers H-W (2024), LIBS for prospecting and Raman spectroscopy for monitoring: two feasibility studies for supporting *in-situ* resource utilization.
Front. Space Technol. 5:1336548.
doi: 10.3389/frspt.2024.1336548

LIBS for prospecting and Raman spectroscopy for monitoring: two feasibility studies for supporting *in-situ* resource utilization

Kristin Rammelkamp[1]*, Susanne Schröder[1]*, Bethany A. Lomax[2], Elise Clavé[1] and Heinz-Wilhelm Hübers[1,3]

[1]Institute of Optical Sensor Systems, German Aerospace Center (DLR), Berlin, Germany, [2]European Space Research and Technology Centre (ESA-ESTEC), European Space Agency, Noordwijk, Netherlands, [3]Department of Physics, Humboldt-Universität zu Berlin, Berlin, Germany

Laser-induced breakdown spectroscopy (LIBS) and Raman spectroscopy are still rather new techniques for *in-situ* exploration of extraterrestrial planetary surfaces but have shown their suitability and great potential in several successful robotic missions already. Next to serving primary scientific applications, both methods can also be used in the context of *in-situ* resource utilization (ISRU) such as scouting for wanted substances and the surveillance of extraction processes. Here, we present two laboratory studies conducted in the context of ISRU with a focus on the chain from prospecting to extracting oxygen from lunar regolith. For LIBS, with optimized data processing and combined with state-of-the-art multivariate data analysis approaches, we show the potential of the technique for identifying samples with increased ilmenite content and for elemental quantification. The measurements were done using lunar regolith simulant and low pressures simulating vacuum on atmosphereless bodies such as the Moon. With Raman spectroscopy, we analyzed lunar regolith simulant samples that underwent electrochemical alteration for oxygen extraction and production of metal alloys demonstrating the potential of Raman spectroscopy for ISRU process monitoring. We also discuss the results in a broader context, evaluating the potential of both methods for other aspects of ISRU support.

KEYWORDS

ISRU, LIBS, Raman, spectroscopy, *in-situ*, Moon

1 Introduction

In recent years, there has been a resurgence of interest and ambition surrounding humanity's return to the Moon (Crawford et al., 2012), driven by a collaborative effort between organizations from both the public and private sectors. Enabling scientific research and exploration while also establishing a long-term and cost-effective robotic and human presence on the Moon will lay the groundwork for future human missions to Mars and beyond. For this, the implementation and optimization of utilizing local resources becomes absolutely necessary. *In-situ* resource utilization (ISRU) will reduce costs, mass, and even risks of the missions and activities by extracting and processing indigenous resources including water, minerals, and gases, for a variety of applications such as life support, construction materials, and propellants for spacecrafts (Anand et al., 2012; Crawford, 2015). Specifically, the most important products from ISRU on the Moon are thought to include

O_2 and H_2O for life support, H_2 and O_2 for fuel and propellant, and other elements and substances for metallurgic and chemical production processes (Anand et al., 2012). The lunar regolith covering most of the Moon's surface with a thickness of several meters presents a likely primary feed stock for ISRU (McKay et al., 1991; Anand et al., 2012). The lunar regolith contains 45 wt% oxygen (Schlüter and Cowley, 2020). One particularly interesting mineral candidate for ISRU and oxygen extraction is the titanium-iron oxide ilmenite ($FeTiO_3$), as the iron oxide it contains can be reduced with hydrogen at a lower temperature compared to other processes. While reliance on ilmenite limits the oxygen yield and the locations on the lunar surface where the process is relevant, hydrogen reduction is one of the most studied ISRU processes (Anand et al. (2012) and references therein). More recently, molten salt electrolysis has been shown to extract almost all of the oxygen from lunar regolith using process temperatures similar to ilmenite reduction, which would allow for the simultaneous extraction of oxygen and metals from lunar regolith at any location (Lomax et al., 2020).

Furthermore, in the context of the increasing demand for technology metals, platinum group elements and rare earth elements (REE) are becoming an interesting target. Their extraction is not only of interest in a lunar context, but also extends to other bodies in the Solar System such as asteroids (Andrews et al., 2015).

The first step in ISRU is the scouting for and identification of wanted and suitable substances and could be done autonomously by robots with appropriate sensors and instruments. As an example, the composition of the lunar regolith is known to be very localized due to only minor lateral mixing processes (Anand et al., 2012) and areas with best suited materials have to be identified. Next, in the realm of ISRU applications, the necessity of process surveillance and control emerges as a critical aspect in ensuring the efficiency, reliability, and safety of resource extraction and utilization processes. The complex nature of the extraction and processing steps, coupled with the inherent challenges of operating in extraterrestrial environments, necessitates meticulous monitoring and control to optimize resource utilization, mitigate risks, and maximize mission success.

Two laser-based methods with high potential for various aspects in the context of ISRU from prospecting to surveying different processing steps are LIBS (laser-induced breakdown spectroscopy) and Raman spectroscopy. Both methods are increasingly used to study geomaterials with laboratory and portable instrumentation, e.g., (Senesi, 2014; Harmon et al., 2017; Jehlička and Culka, 2022; Senesi et al., 2021), and have entered the field of space exploration within the last decade being successfully applied in mobile robotic missions for *in-situ* analysis on other bodies of the Solar System such as on Mars, see below for more information and references. LIBS and Raman spectroscopy can both be applied with optical access only and without the necessity of sample preparation. Moreover, both methods are widely used for process surveillance and control in terrestrial applications across various industries facilitating real-time monitoring and optimization of different processes, e.g., Noll et al., 2014; Pedarnig et al., 2021.

Raman spectroscopy is a vibrational spectroscopy method that provides fingerprint information about molecular or lattice structure, allowing the identification of compounds and the analysis of crystallographic properties. Raman spectroscopy can be used to analyse minerals, detect impurities, and monitor the progress of chemical reactions or mineral transformations during extraction processes. Raman spectroscopy analyses the small fraction of laser light that is inelastically scattered by the sample and therefore undergoes an energy change, providing information about structure and bonding. Raman spectroscopy had its debut in space exploration with the ultraviolet Raman spectrometer SHERLOC (Bhartia et al., 2021) and the time-resolved Raman spectrometer as part of the SuperCam instrument suite (Wiens et al., 2021; Maurice et al., 2021) both on the Perseverance rover of NASA's Mars2020 mission. The Raman spectrometer called RAX (Hagelschuer et al., 2022; Schröder et al., 2023) for the small rover for JAXA's Martian Moons eXploration (MMX) mission (Michel et al., 2022; Ulamec et al., 2023) that will explore the surface of Mars' moon Phobos, will only be the third Raman spectrometer for extraterrestrial applications, scheduled to launch in 2026. RAX is a particularly compact, low-mass Raman instrument with a volume of only approximately 1 dm^3 and a mass of 1.5 kg. Another Raman spectrometer called RLS was developed for ESA's ExoMars rover (Rull et al., 2017).

LIBS is a technique that allows rapid *in-situ* multi-elemental analysis with no sample preparation and only optical access, making it particularly suitable for exploration tasks. LIBS is particularly sensitive to various metals, including light elements such as hydrogen, and a measurement can be made in seconds. LIBS uses a pulsed, focused laser to ablate a small amount of sample material and create a luminescent microplasma. The plasma emission has characteristic emission lines from which the qualitative and quantitative elemental composition of the sample can be deduced. LIBS is particularly well suited for geomaterial analysis and is increasingly used for both terrestrial, e.g., Rammelkamp et al., 2021; Müller et al., 2021, and extraterrestrial applications. LIBS is being used for *in-situ* geochemical analysis on Mars by NASA's two active rovers: The first LIBS instrument in space exploration is the ChemCam instrument on Curiosity, which has been collecting LIBS data from Gale Crater since the rover's landing in 2012 (Maurice et al., 2012; Wiens et al., 2012; Maurice et al., 2016). With the SuperCam instrument suite on Perseverance, the second LIBS for extraterrestrial purposes has been active in Jezero Crater since landing in 2021 (Wiens et al., 2021; Maurice et al., 2021). One third LIBS instrument on a Mars rover was developed by the Chinese space agency CNSA with MarSCoDe (Xu et al., 2021; Wan et al., 2021) and collected data between late 2021 and 2022. A LIBS instrument was also developed as a payload for the small lunar surface exploration rover of the Indian Chandrayaan-2 mission (Laxmiprasad et al., 2013). While Chandrayaan-2 was not successful due to the lander failing to make a soft landing in 2019, India's follow-up mission succeeded in reaching the Moon. The Chandrayaan LIBS instrument is particularly light-weight with less than 1.2 kg, has no focusing system and measures the lunar regolith beneath the rover's chassis at a constant distance of 0.2 m. For Mars, a high-performant LIBS instrument is currently being developed for space aiming for a mass below 2 kg (Rapin et al., 2023). More LIBS instruments for the Moon were proposed and developed such as the VOILA (Volatiles Identification by Laser Analysis instrument) instrument for the LUVMI-X (Lunar Volatiles Mobile Instrumention - Extended) rover which was - as the

names suggest - specifically designed for volatile analysis with a focus on hydrogen detection (Losekamm et al., 2022; Vogt et al., 2022a). LIBS instruments such as ChemCam and SuperCam are comparatively large (≈20 L) and heavy (≈10 kg), but are very flexible with their telescopic systems and can measure samples at a wide range of distances of up to 7 m (Maurice et al., 2012; 2021; Wiens et al., 2012; 2021). LIBS instruments for ISRU may be smaller, which may require compromises with regard to their performance and versatility, e.g., in tuning them to specific use cases while reducing their utility to others. The size, mass, and energy consumption of LIBS instruments are dependent on whole mission concepts, on the objectives, the hosting platforms, working distances, *etc.*, and cannot be specified in general terms. As an example, power consumption of the existing space LIBS instruments ranges from less than 5 W (Chandrayaan) to several tens of watts. It is important to note that the characteristics of the laser-induced plasma strongly depend on ambient conditions, such as pressure (Effenberger and Scott, 2010). For laboratory studies, these have to be simulated experimentally in vacuum chambers. It was found that while Martian atmospheric conditions are close to ideal, also in lower pressures such as on the Moon and other bodies without an atmosphere, suitable LIBS data can be obtained (Lasue et al., 2012; Kubitza et al., 2020; Vogt et al., 2022a).

While in a previous study, we have focused on hydrogen detection and its quantification in a lunar context (Vogt et al., 2022a), the focus of this work is on two aspects of the oxygen extraction chain and how LIBS and Raman spectroscopy could support ISRU activities. We optimize data processing and analysis of the LIBS data obtained in vacuum with state-of-the-art multivariate data analysis approaches and show the capability of LIBS for identifying and potentially quantifying enrichments of ilmenite in lunar regolith simulant. Moreover, we demonstrate the capability to survey the progression of oxygen extraction and metal alloy production with Raman spectroscopy, using samples of lunar regolith simulant reduced by molten salt electrolysis. The results are discussed in a broader context of the potential for ISRU supporting applications of both methods comparing to the state-of-the art.

2 LIBS

2.1 Experimental setup: LIBS breadboard model VOILA

LIBS data were measured with a breadboard model of an instrument called Volatiles Identification by Laser Analysis instrument (VOILA) which was developed as payload for a lightweight rover for *in-situ* exploration of the lunar south pole. The initial design and development of this rover and its payload was part of the Lunar Volatiles Mobile Instrumention - Extended (LUVMI-X) project (Losekamm et al., 2022; Vogt et al., 2022a) describe the VOILA breadboard model in detail and the choices made in its design. We would like to refer to this work for more details on the VOILA instrument and provide only the most relevant information below.

The samples are placed in a vacuum chamber which can be evacuated to pressures lower than 10 mPa to simulate the low pressure on the surface of the Moon. In this pressure range, the mean free path is large enough for the LIBS plasma to expand freely without being confined by the surrounding atmosphere. Going to even lower pressures such as on the surface of the Moon (Heiken et al., 1991) is expected to not change the behaviour of the laser-induced plasma so that experiments simulating the vacuum of atmosphereless bodies are typically done in the range of 10–100 mPa (Knight et al., 2000; Lasue et al., 2012; Kubitza et al., 2020). The laser was developed by the Laser Zentrum Hannover e.V. (LZH) in the framework of the LUVMI-X project. The active medium is a Yb:YAG crystal emitting at a wavelength of 1,030 nm with a pulse duration of 7.8 ns. The energy per pulse is adjustable up to a maximum of 25 mJ. The optical head where the laser beam is expanded was built of commercial off-the-shelf components (COTS). The expanded beam is then focused inside the simulation chamber onto the sample at a working distance of 400 mm. The emitted radiation by the plasma is collected by the same optics which is used for the focusing of the laser beam. Within the optical head, a dichroic mirror separates the two light paths and the collected plasma radiation is guided to a fiber-coupled compact spectrometer (Avantes, model AvaSpec-Mini). With a spectral resolution of about 0.4 nm, the spectrometer covers a spectral range of 340–900 nm, from which we use only the range 390–800 nm as before 390 nm and beyond 800 nm the transmission of the optical head is limited. As previously noted, the instrument design decisions are discussed in Vogt et al. (2022a) and are not part of this study. However, we want to comment on the smaller spectral range compared to instruments such as ChemCam and SuperCam. These instruments were designed for different purposes and missions. VOILA has to be much smaller and lighter, which limits the choice of spectral range, in which we ensured that the chosen range includes emission lines from the majority of oxides in lunar material (Si, Al, Ti, Fe, Mg, and Ca), as well as from alkali elements (Na, Li, and K) and H and O.

2.2 LIBS samples and sample preparation

For the study on the potential of detection and quantification of ilmenite enrichments in lunar regolith with LIBS, two commercially available lunar regolith simulants were mixed with concentrated ilmenite which was provided by the Museum für Naturkunde Berlin (MfN). The lunar regolith simulants representing the Lunar mare composition (LMS-1) and the Lunar highland composition (LHS-1), respectively, are both from Exolith. The mineral and oxide composition is given in Table 1. In their pure form, LHS-1 contains 0.4 wt% and LMS-1 4.3 wt% of ilmenite. All three components are available in form of fine to coarse grained powders and were mixed and further crushed with mortar and pestle. The resulting mixtures with varying ilmenite concentrations were pressed into pellets of about 1 g and 14 mm diameter at a pressure of 5 t for about 10 min. We produced 15 and 14 samples per simulant, respectively, one pure sample of both simulants and one pure ilmenite sample, giving a total of 32 samples, an overview of which is given in Table 2.

TABLE 1 Overview of both mineralogical and elemental oxide composition of the two lunar regolith simulants LMS-1 and LHS-1 used in the LIBS experiments. The LMS-1 is also the starting material of electrolysis samples measured with Raman spectroscopy. Trace elements such as Cl, Cr_2O_3, NiO, SO_3, and SrO are not shown.

Mineral component	wt% LMS-1	wt% LHS-1	Oxide	wt% LMS-1	wt% LHS-1
Pyroxene	32.8	0.3	SiO_2	40.2	48.1
Glass-rich basalt	32.0	24.7	TiO_2	7.3	1.1
Anorthosite	19.8	75.4	Al_2O_3	14.0	25.8
Olivine	11.1	0.2	FeO	13.9	3.7
Ilmenite	4.3	0.4	MnO	0.3	0.1
			MgO	12.0	0.3
			CaO	9.8	18.4
			K_2O	0.6	0.7

TABLE 2 Overview of samples measured with LIBS.

Component	# of samples	Pure ilmenite [wt%]	Range of ilmenite concentrations [wt%]
LMS-1	15	4.3	4.3–52.0
LHS-1	16	0.4	0.4–39.5
Ilmenite	1	100	-

2.3 LIBS measurements

All mixtures of lunar regolith simulants with ilmenite were measured with the VOILA setup described in Section 2.1. The pressure in the vacuum chamber was reduced to below 10 mPa. Each sample was measured at ten different locations by moving the sample holder. The laser was started with a repetition rate of 10 Hz together with the spectrometer with an exposure time of 3 s, i.e., the emission of 30 successively laser-induced plasmas was accumulated for one spectrum at one position. A dark spectrum was measured with the same exposure time for each sample and used for all ten spectra. The laser pulse energy was adjusted to 17 mJ.

2.4 LIBS data preprocessing and analysis

Before the analysis, several preprocessing steps were applied. For all ten measurements on one sample, one dark spectrum was measured which is subtracted from the LIBS active data first. Then, all spectra are corrected for the response function of the spectrometer and the transmittance of the optical head. The mostly undiagnostic continuum emission of the laser-induced plasma that is superimposing the emission lines of the atoms and ions was removed computationally by performing background subtraction. This was carried out iteratively by first smoothing the spectrum and subsequently masking all un-smoothed spectrum values that are larger than the smoothed ones. When repeating this procedure multiple times, a satisfactory fit of the background can be achieved without affecting the emission line intensities. A more detailed description of the baseline correction can be found in the Supplementary Material.

As part of our initial exploration of the data, we used the multivariate technique principal component analysis (PCA) on all of the spectra. PCA is a matrix decomposition technique in which the data is rotated into a new space where the majority of the variation in the initial data can be represented by a reduced number of dimensions, termed as components (Lever et al., 2017). Applied to LIBS data, it is in particular useful to group similar spectra together, investigate correlations, and to check for outliers (Pořízka et al., 2018). In our study, it was seen that the amount of explained variance increases at a slow rate as additional components are added. The initial four components account for 61% of the variance, however, subsequent components result in only marginal increments. This trend implies the presence of uncorrelated noise among the spectra and gave rise to the approach of using the first four components to denoise the spectra, which is a common approach in spectral data processing, e.g., Stephan et al. (2008). We then applied this method, taking into account four components, and obtained eigenvalues, also called scores, for each spectrum. Finally, we used the model to back-transform these eigenvalues, resulting in notably cleaner spectra. An example is shown in Figure 1, which shows the original spectrum, the reconstructed spectrum and, in the lower plot, the residuals. The residuals show no spectral characteristics, indicating the successful removal of noise in the back-transformation.

2.5 LIBS ilmenite detection

For a better understanding of the measured LIBS data, we first looked at the spectra of pure LMS-1, LHS-1 and ilmenite. The average spectra of the ten measurements were taken and are shown in Figure 2. The top row shows two zooms to spectral regions with

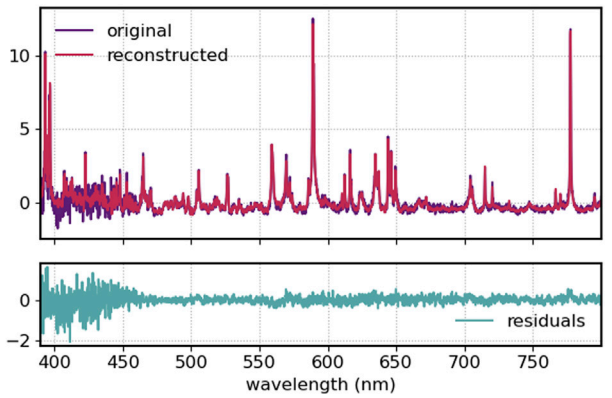

FIGURE 1
Example spectrum of an LHS-1 sample, original spectrum and back-transformed using a four-dimensional PCA model. The bottom plot shows the residuals between the original and reconstructed spectrum. The reconstructed spectrum is reduced in noise but not in spectral information, as can be seen from the residuals.

strong Ti emission lines. Fe emission lines can also be observed in the ilmenite spectrum, but they are weaker than the Ti lines. The LMS-1 spectrum shows very weak Ti emission lines even though it contains 4.3 wt% ilmenite. In general, both spectra of LMS-1 and LHS-1 have a few weak features in the regions with strong Ti emission lines, 452–458 nm and 497–504 nm. However, they are difficult to interpret because they cannot be clearly distinguished from noise. The main difference between the two lunar regolith simulants lies in the strength of the Mg and Ca emission lines: The LMS-1 spectrum has stronger Mg emission lines, whereas the LHS-1 spectrum has stronger Ca emission lines, consistent with their compositions, compare Table 1.

Two approaches to the identification and prospective quantification of ilmenite enrichments were investigated. In the first, all counts in the spectral range 496.5–503.0 nm were summed, as most of the intensities there are expected to be from Ti. Although ilmenite also contains Fe, we decided to focus on Ti because Ti emission lines are more prominent in the instrument's spectral range than those of Fe, see Figure 2. From a geological perspective, Ti is a better indicator of the presence of ilmenite than Fe, since Fe is a major constituent in most geological materials. For this approach, the calibrated spectra were used but no standardization or data normalization was applied.

The second approach is based on the matrix decomposition technique non-negative matrix factorization (NMF), which was applied to the entire data set with the aim of extracting a factor that can be assigned to ilmenite. NMF belongs to the family of source separation techniques and assumes nonnegativity in the data set which makes it in particular useful for data with a physical interpretation (Pauca et al., 2006). An NMF model with four factors can reconstruct the data with a reconstruction error of 6.7%. We also tested models with more factors, but this resulted in only a small reduction in the reconstruction error, while the factors modelled more noise. We also applied NMF to the data that had not undergone PCA denoising. This also showed that clear

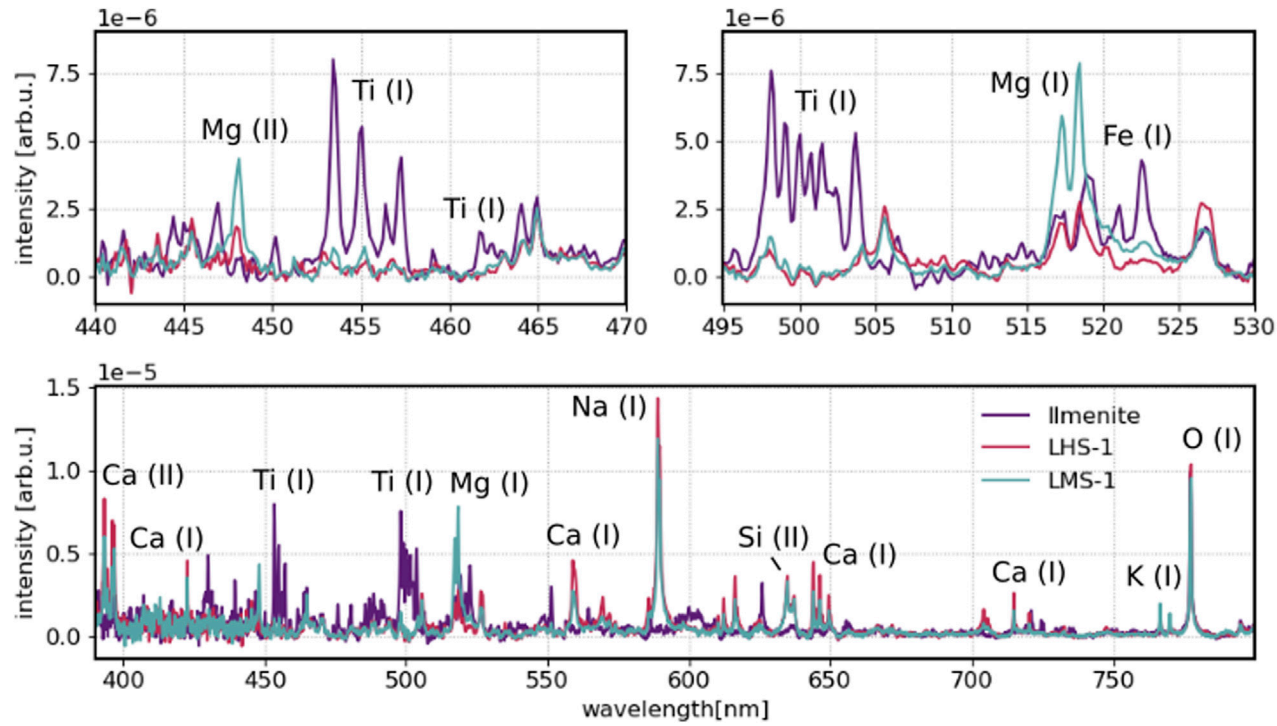

FIGURE 2
Mean LIBS spectra of pure LMS-1, LHS-1 and ilmenite samples. The lower plot shows the full spectral range used in this study. The most prominent emission lines are annotated. Major differences between the three samples are observed for the Ca, Mg and Ti emission lines. The plots in the top row zoom in on the spectral regions with the strongest Ti emission lines indicative of ilmenite.

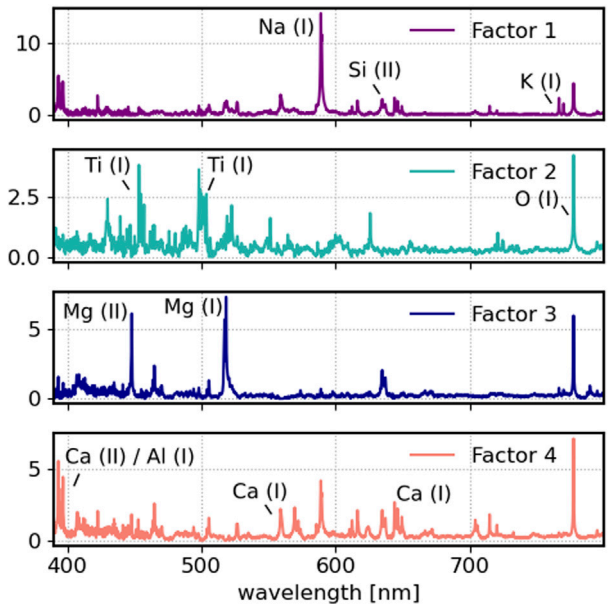

FIGURE 3
All four factors of the NMF model with annotations of the most prominent emission lines on each factor. Factor 2 can be interpreted as the ilmenite component showing dominant Ti emission lines while factor 3 and factor 4 represents LMS-1 and LHS-1 components, respectively.

factors were difficult to identify as they were characterized by noise variations. Finally, we decided on the four-factor model whose extracted factors are shown in Figure 3. The first NMF factor primarily represents the alkalis Na and K, and Si, which are present in comparable quantities in both lunar regolith simulants. Thus, this factor may be interpreted as a shared baseline. The NMF factor 2 can be assigned to ilmenite mainly on the basis of strong Ti emission lines. Factor 3 represents the LMS-1 component with strong Mg lines, while dominant Ca emission lines on factor 4 indicate a correspondence with the LHS-1 component. This is confirmed by the fact that the majority of LHS-1 samples have the highest scores on factor 4 and the same can be observed for LMS-1 samples and factor 3.

In Figure 4, for each sample except the pure ilmenite sample, the summed Ti intensities and the scores on NMF factor 2 are plotted versus their known ilmenite concentration. Both values are shown as box plots, where each box corresponds to one sample and contains the values of all ten measurements. For both approaches, an overall increase of the ilmenite measure is observable with increasing ilmenite concentrations. However, the values show in both cases a large scatter and also a few targets which do not follow the overall increase. Since the scatter is observable for both approaches, the reason is likely related to the samples and the measured data and not to the data analysis approach. Also worth mentioning is that no clear trends were observed when looking at the two lunar regolith simulants separately from each other.

Although the components were crushed and mixed with mortar and pestle, the samples are not homogeneous on the scale of the ablation zone, i.e., the laser spot size. To investigate this, images of the samples were taken using a digital microscope, a selection of which are shown in Figure 5. For both simulants, the pure sample, a sample with medium and a sample with high ilmenite enrichment are shown. The ilmenite grains can be recognised by the fact that they are black and reflective. As expected, the density of the ilmenite grains increases with increasing concentration. Their distribution is not homogeneous and the grains also differ in size. In a recent study, regolith simulants from Exolith Lab including the two lunar simulants used for the LIBS samples LMS-1 and LHS-1 were extensively investigated and their production process described in detail (Long-Fox and Britt, 2023). Besides the mineralogical composition, the physical properties of the simulants including the grain size distribution were designed to match Apollo samples. The grain size in both samples vary in a range of $< 0.04\ \mu$m–1,000 μm. To compare this to our LIBS investigated spot sizes, we also investigated the craters that are left after a LIBS measurement (not shown). These craters generally vary somewhat in size with smaller or larger grains removed from the crater edges and have an average diameter of 500 μm and a typical depth of 200–500 μm when formed by 30 consecutive laser shots and the subsequent plasma.

With the observed heterogeneity of the samples, it is therefore not surprising that with increasing concentration of ilmenite, the scatter of the points increases. At a higher density, the probability is higher that several of the ten points measured on a sample mainly hit ilmenite grains. Accordingly, we have introduced a measure for both approaches that is closer to the reality of heterogeneous geological samples: we count how many points of all points measured on a sample have a clear signature of ilmenite. The definition of a clear signature in our case is empirical for which the definition of the limit of detection was followed, but adapted to the measurement data. Instead of a true blank sample, samples with an ilmenite concentration of less than 5 wt% were considered as samples without a clear signal. This included 4 samples with a total of 40 measurements. The threshold for a clear signature was then calculated by taking the mean value plus 3 times the standard deviation of these 40 measurements for both summed Ti intensities and NMF 2 scores. For the summed Ti intensity, we obtained a value of 2.0×10^{-5} as the limit, see purple dashed line in Figure 4 upper plot. For the NMF Factor 2 score, the limit is at 0.1, indicated by the turquoise dashed line in the lower plot of Figure 4. All measurement points that have a value above these limits are counted as ilmenite detections. The plots in Figure 6 display the rate of ilmenite detections for each approach as ilmenite concentrations increase. Both approaches show an increase in ilmenite detections, with the highest rates occurring predominantly in samples with a concentration greater than 30 wt% ilmenite. Furthermore, the NMF factor 2 approach begins to detect a significant number of occurrences at approximately 10 wt% ilmenite. The summed Ti intensity is less responsive to increments in ilmenite concentration as there is still one sample with zero ilmenite detections while these samples have ilmenite concentrations greater than 10 wt%. Although this dataset exhibits heterogeneity that precludes reliable quantification of ilmenite abundances, the approach based on the extracted NMF factor can be inferred as a type of lower detection limit for ilmenite enrichments. Two or more detections of ilmenite within a raster containing ten points may indicate that this target or area possesses an average ilmenite enrichment greater than 10 wt%.

Overall, both approaches have their advantages and disadvantages for the detection of ilmenite with LIBS. While the summation of Ti intensities is relatively easy to implement, it is not guaranteed that lines from other elements found in the same spectral range do not influence the results. The lines do not even have to be

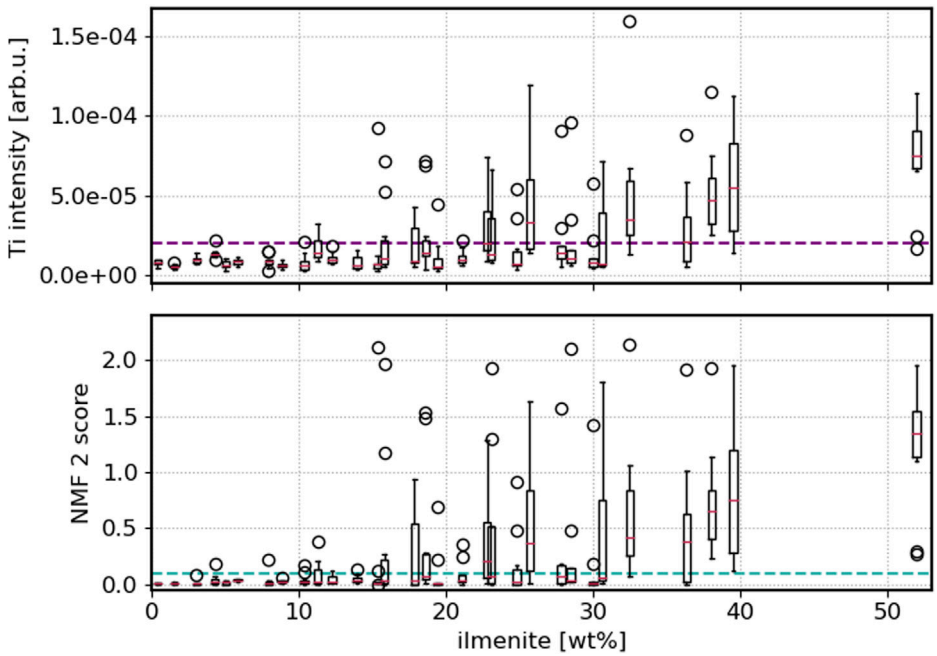

FIGURE 4
For both approaches, the summation of Ti intensity and NMF factor 2 values, are shown as a function of ilmenite concentration in the samples. For each sample a box is shown, as known from conventional box plots, containing all 10 measurements from one sample. The dashed lines correspond to the thresholds defined to discriminate between ilmenite not being detected and ilmenite detected. In both cases there is a general increase with increasing ilmenite concentration, but what increases more is the scatter between the 10 measurements on a sample.

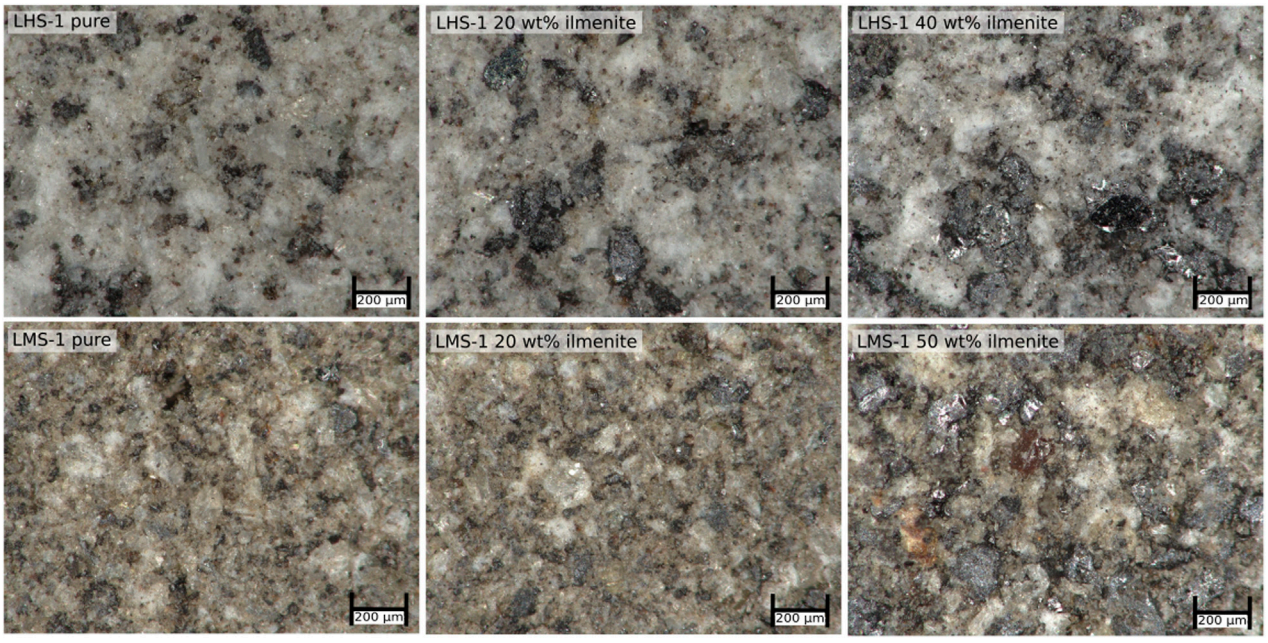

FIGURE 5
Images of selected samples taken with a digital microscope. For each lunar regolith simulant, the pure samples, a sample with a moderate addition of ilmenite, and the sample with the largest amount of ilmenite added are shown. In general, it can be seen that the samples are heterogeneous. In addition, the shiny metallic grains that are ilmenite are not evenly distributed and it is very likely that the laser is not hitting ilmenite grains in each measurement, although the overall ilmenite abundance may be high.

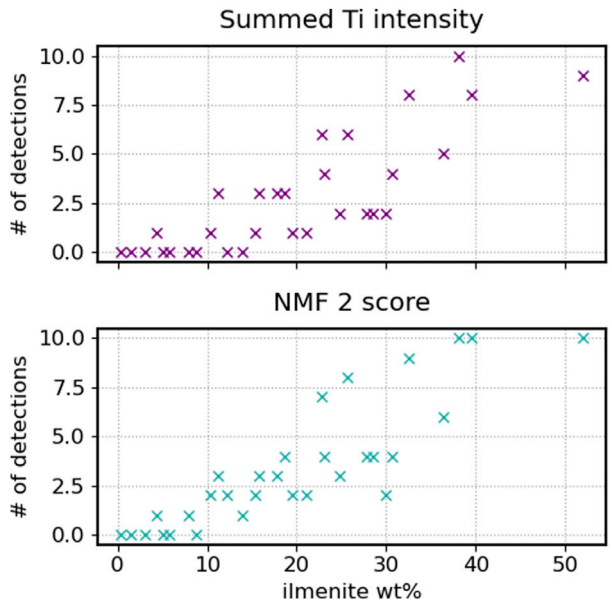

FIGURE 6
Number of ilmenite detections per sample and therefore per ilmenite concentration for both approaches. Starting with samples with more than 10 wt% of ilmenite, the number of ilmenite detections increases with increasing ilmenite concentration. However, the increase is not continuous and some samples have less detections than samples with lower ilmenite abundances.

particularly strong and directly recognisable to influence the results. On the other hand, extracting a suitable component with methods like NMF that can mainly be assigned to ilmenite minimizes the risk of taking into account influences from other elements. How this approach can be applied to a more comprehensive and realistic data set with enhanced mineral diversity of the samples and in particular the effects of variations in iron content needs further investigation. LIBS detects elements rather than minerals, which means that other Ti-bearing minerals may also contribute to the detection, potentially biasing the ilmenite result. However, previous analyses of the lunar surface have shown that Ti is mainly present in the mineral ilmenite, and less frequently in Si-Ti phases such as silcate glasses (Lucey et al., 1998; Anand et al., 2012). Additionally, as previously mentioned, the NMF approach is less influenced by other elements. To achieve a high score on NMF factor 2, all Ti lines must be present. and lines that are not part of the factor, such as Si (see Figure 3), do not count. In closing, this study yielded promising results that LIBS is indeed suitable for *in-situ* detection and quantification of ilmenite enhancements in lunar regolith with dedicated data processing and state-of-the-art multivariate data analysis.

3 Raman

3.1 Experimental setup: Confocal Raman microscope

The experiments were performed with a commercial confocal and continuous-wave (cw) Raman microscope (WITec alpha300 R system) at DLR Berlin, Germany. A frequency-doubled cw Nd:YAG laser with an excitation wavelength of 532 nm was used. The laser radiation was focused to a spot of approximately 1.5 μ m diameter on the sample surface using a Nikon ×10 objective. An edge filter which opens around 70 cm^{-1} suppresses the detection of Rayleigh scattered photons. The spectrometer covers a spectral range up to 3,800 cm^{-1} and has a spectral resolution of about 4 cm^{-1}.

3.2 Raman samples and sample preparation

To demonstrate one use case for Raman spectroscopy in the context of ISRU, a sample set that was chemically altered in an electrochemical FFC (Fray, Farthing, Chen) process (Chen and Fray, 2020; Schlüter and Cowley, 2020) for oxygen extraction was chosen. In recent studies by Lomax et al. (2020) and Meurisse et al. (2022), the FFC process was demonstrated for the direct electro-deoxidation of solid-state lunar regolith simulant. Besides the process, also the development of inert anodes is an important research area (Hu et al., 2016; Du et al., 2021) to ensure that there are deployable models in space when the process is ready for use on the Moon. For our study, samples that had undergone the FCC process using the experimental set up described in Meurisse et al. (2022) were measured with Raman spectroscopy. This set of samples contained lunar regolith simulant at different stages throughout the process, with successively less oxygen and more metals.

The starting material for all samples was the lunar regolith simulant LMS-1 (Exolith Lunar Mare Simulant, procured in 2019), of which the composition can be seen in Table 1. The untreated LMS-1 starting material was used as a reference and contains approximately 42 wt% oxygen. Five samples that spent different lengths of time in the electrolysis process were analysed. The samples are therefore labelled: 00, 05, 10, 13, 16, 24 h. Following 24 h of processing, approximately 80% of the oxygen had been removed from the LMS-1 material. Similar to the LIBS samples (Section 2.2), the samples were pressed into pellets.

3.3 Raman measurements

All measurements were carried out with the same measurement parameters. We made single measurements on the samples but also line scans where mostly eight points were measured on a line previously drawn in the microscope image of the samples. For both the single measurements and the line scans, the Raman signal was integrated for 5 seconds and no further accumulations were made. The laser power was set to 7 mW for all measurements. The number of measurements per sample varied, but a minimum of 33 spectra per sample were acquired from all. A detailed list is given in Table 3.

3.4 Raman data preprocessing

Not all measured spectra show Raman signatures and also varying contributions of luminescence were observed. The observed luminescence was deemed undiagnostic for this study and the broad superimposing emission was therefore removed in

a first data preprocessing step with a baseline subtraction. For this, we employed the asymmetrically reweighted penalized least squares algorithm which is based on the Whittaker smoother (Baek et al., 2015). The subtraction of the baseline is not crucial for the subsequent evaluation, however, for more information on the methods used see the Supplementary Material. To filter out spectra without relevant Raman signatures, a criterion based on signal-to-noise ratio was used. The maximum signal value in the spectrum was picked and the ratio of its height to the standard deviation of a nearby peak-free area in the spectrum was taken. After analyzing the ratio and examining the spectra, we decided that a ratio of eight was a reasonable threshold, so that spectra with a ratio greater than eight were kept for further analysis. The final numbers of spectra per sample are also listed in Table 3.

3.5 Raman results

The analysis of the Raman spectra is mainly based on qualitative observations, i.e., the identification of minerals and components in each sample. We first present examples of spectra and corresponding mineral identification in the starting and end materials (00-h and 24-h samples). We then observe the evolution of the identified Raman signatures throughout the series, to monitor the changes happening in the sample during the process.

Note that the material analyzed in the current study is not the most ideal material for Raman spectroscopy. Lomax et al. (2020) showed that the final material consists predominantly of metal alloys that are weak Raman scatterers. Consequently, several Raman spectra of the treated samples expectedly do not exhibit any detectable Raman signal, see Table 3. In spite of this we have observed several spectra with significant Raman signatures.

Starting with the Raman spectra of the untreated sample, it was possible to identify Raman spectra of minerals that match the known mineralogical composition of the starting material. The upper part of Figure 7 shows an image of the sample taken with the microscope together with the course of a line scan and Raman spectra of three highlighted positions. At position 1, a plagioclase spectrum was measured, at position 2 an olivine spectrum and at position 3 a pyroxene spectrum. These minerals are consistent with the mineralogical composition of the starting material (Table 1). The sample that was in the electrolysis for the longest time, 24 h, shows very different signatures. The lower part of Figure 7 shows a picture and also three selected Raman spectra of this final sample. Looking at the microscope image alone, it is noticeable that the parts of the sample are more reflective and look more metallic overall compared to the untreated sample. The spectrum of position 1 shows spectra of three components: silicon, carbonate, and graphite. Raman modes of these materials also occur at position 2 with both silicon and graphite modes, and at position 3 with the modes of graphite alone.

The comparison of the initial and final samples demonstrates that Raman spectroscopy has the potential to assist in controlling the results of the oxygen extraction process. Moreover, Raman may also be applicable *in-situ* for real-time monitoring of the process. In this instance, it would be possible to measure several tens of spectra and use the statistics of these spectra to monitor the evolution of the sample. Based on our investigation of the starting and end material, we identified the occurrences and characteristics of different signatures in the series.

First, we track the minerals identified in the starting material: olivine, pyroxene and plagioclase. Considering these minerals as characteristic of the starting material, their presence was monitored in the treated samples and the results are displayed in the last column of Table 3. Keeping in mind that all samples are mixtures and heterogeneous on the scale of the Raman laser spot size, and that it is always possible that we have not measured relevant phases, it can still be observed that the number of starting material mineral detections decreases significantly for the 5-h sample. Only two additional olivine spectra were measured for the later samples. This suggests that despite incomplete oxygen extraction for these samples, the starting material has already been altered to a considerable degree after 5 h of electrolysis.

Secondly, the Si mode around 500 cm^{-1} is visible in numerous spectra of the treated samples and will be discussed in more detail in the following. The Si mode appears mainly around 500 cm^{-1}, for example, also in the spectrum measured at position 2 (lower part of Figure 7). For crystalline silicon one would expect a sharp peak around 520 cm^{-1} associated to a transversal optical phonon. The mode that we observe in our study is shifted towards lower Raman shifts and broadened which could indicate that the silicon is in a more amorphous than crystalline phase (Zwick and Carles, 1993). For the samples which spent 5, 13 and 24 h, respectively in the electrolysis process, the Si mode is shown in the upper part of Figure 8. The gray lines belong to spectra of each of the samples which exhibits a clear Si mode whereas the pink line is the mode of crystalline Si measured on a Si wafer with the same experimental set-up. All spectra were normalized to their maximum intensity for better comparison. The comparison clearly shows that the Si Raman modes of the reduced lunar regolith simulant samples are broadened and also shifted to lower Raman shifts. To investigate whether the magnitude of the shift and the line width is related to the time the samples spent in electrolysis, we fitted the modes with Voigt profiles and checked their line center as well as their width via the full width at half maximum (FWHM). The lower part of Figure 8 shows the results as violin plots for all spectra having the Si mode. The violin plots display the distributions of both fit parameters for each sample where the middle horizontal line represents the median. There is no distinct trend observable with regard to the duration, nevertheless some differences appear. Regarding the peak positions (shown in the lower left of Figure 8), the 5 and 10-h samples with the shortest duration have mainly peak positions larger than 510 cm^{-1} and smaller than 520 cm^{-1}. A larger spread of center positions can be observed for the 13 and 16-h samples, reaching from 490 cm^{-1} up to 520 cm^{-1}. The 24-h samples with the longest duration in the electrolysis feature center positions that are again less scattered but are mainly at a lower Raman shift close to 500 cm^{-1}. The Si mode widths (shown in the lower right of Figure 8) for samples electrolysed for 5 and 10-h are on average narrower than those for longer duration samples. The 13 and 16-h samples exhibit wider distributions, while the Si mode widths for the 24-h sample are less dispersed, but larger than those for the 5 and 10-h samples. The observed variations in center position and width suggest that a Si phase with varying degrees of crystallinity could have emerged during electrolysis. Amorphous silicon has a broad peak

TABLE 3 Overview of Raman spectroscopy measurements on the different treated samples including the starting material. Not all spectra exhibit identifiable Raman modes; therefore, not all spectra were kept for further analysis as described in the text. The rate shown is for the remaining spectra. The last column gives the number of measured spectra which could be assigned to primary minerals characteristic of the starting material, i.e., to pyroxene, plagioclase or olivine.

Sample	# of measurement points	# of proofed spectra	Rate [%]	# of primary minerals spectra
00 h	34	12	35	10
05 h	33	27	82	7
10 h	41	29	71	0
13 h	34	23	68	1
16 h	49	42	86	1
24 h	50	38	76	0

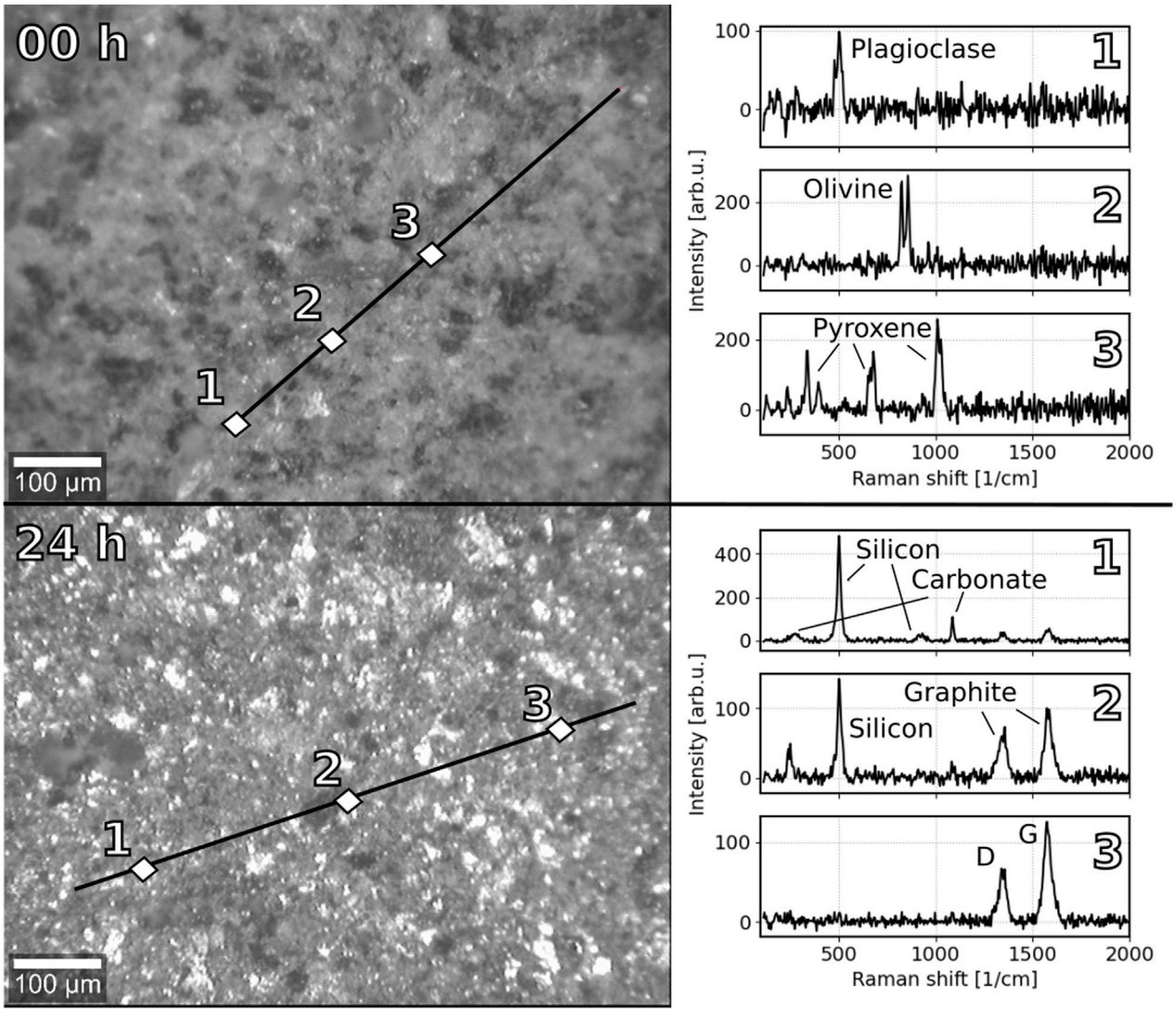

FIGURE 7
Examples of the untreated (top) and the 24-h sample (bottom) viewed through the Raman microscope. The 24-h sample reveals an increased presence of reflective sections, typically observed in metallic substances. In both images, the black line marks the course of a linescan with three positions highlighted. The corresponding Raman spectra from these positions are displayed on the right. While the untreated sample displays spectra of minerals belonging to the initial material, the 24-h sample spectra may be interpreted as results of the electrolysis process.

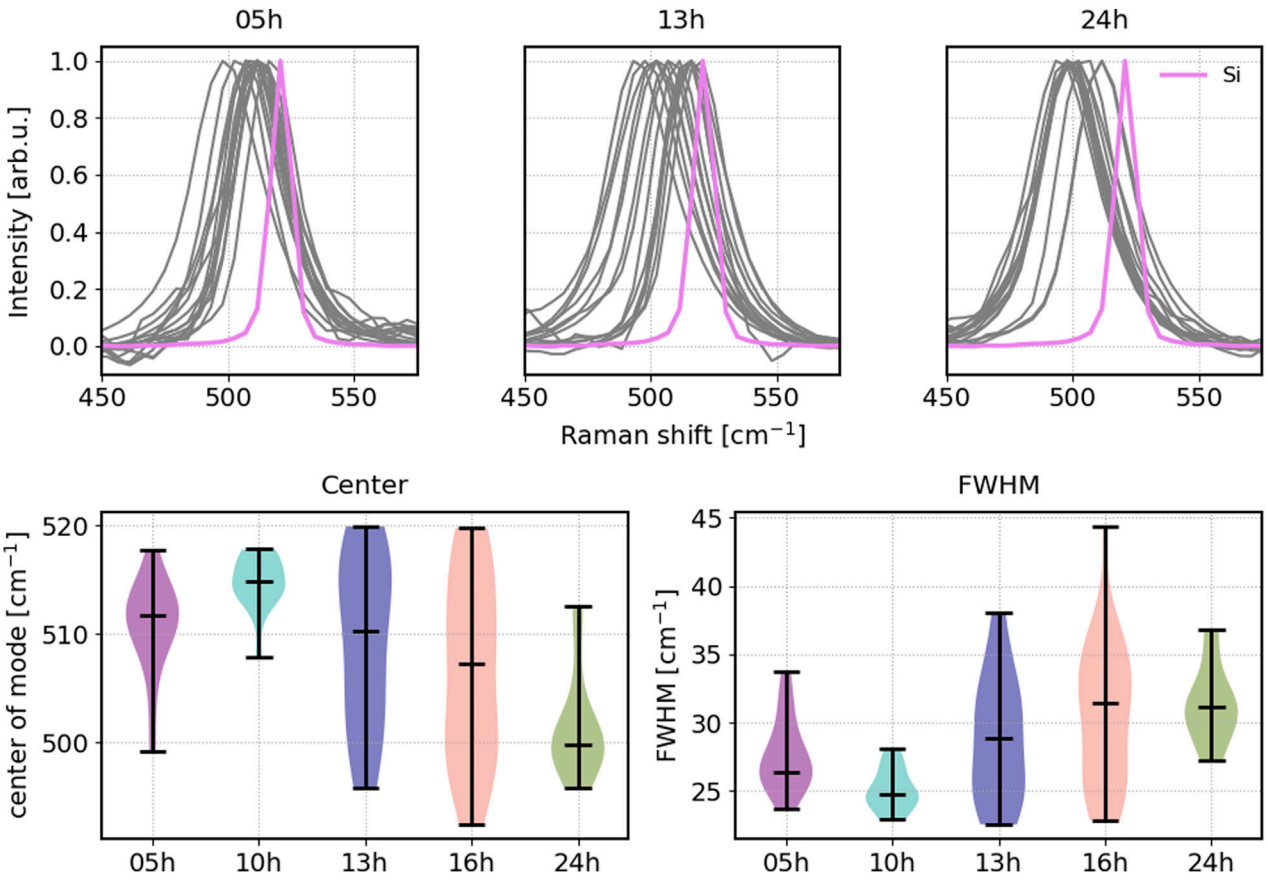

FIGURE 8
Investigation of Si Raman mode at 520 cm^{-1}. *Top row*: Zoom for spectra measured on the 5, 13 and 24-h samples (gray lines), only spectra with a clear Si mode are shown. For comparison, the Si mode measured on a Si wafer with the same set-up is shown in pink. All spectra were normalized to their maximum intensity. *Bottom row*: Mode fitting results as violin plots where the middle horizontal line represents the median. *Left*: The center is at higher wavenumbers on average for the 5 and 10-h samples than for the 24-h sample, while a wider distribution for the 13 and 16-h samples than for the others is observable. *Right*: Also, the broadening indicates variations among the samples: there is again a more extensive spread observed for the 13 and 16-h samples, whereas the Si modes of the shorter duration samples are narrower when compared to those of the 24-h sample.

around 480 cm^{-1} and depending on the crystalline fraction, it overlaps more or less with the crystalline Si mode at 520 cm $^{-1}$ resulting in shifts to lower Raman shifts (Kimura and Katoda, 1997; Islam and Kumar 2001). Several studies have investigated the impact of strain and stress on both crystalline and amorphous silicon, and have explored how these influences affect the Raman Si modes (Ureña et al., 2013; Strubbe et al., 2015). However, in order to make conclusive interpretations from our samples and to potentially link the Si mode to the amount of extracted oxygen, further research would be necessary that specifically targets the Si phases.

Finally, we observed the appearance of carbon-related features. Carbonate is identified by the A_{1g} mode of the CO_3 polyhedra at 1,085 cm^{-1} (Dufresne et al., 2018). Graphite is observable in all of the three selected spectra of the 24-h sample shown in Figure 7 by means of the so called D and G modes at 1,370 cm^{-1} and 1,580 cm^{-1}, respectively. The G mode is the typical E_{2g} mode of sp^2 carbon systems due to stretching of C-C bonds while the D mode was named for disorder-induced-mode (Reich and Thomsen, 2004). Graphite is formed as a result of degradation of the graphite anode utilized in the electrolysis process. In the spectrum of the 10-h sample, graphite modes can be observed for the first time, while no graphite spectrum was measured from the 13-h sample. The modes appear quite regularly for the 16 and 24-h samples as expected because of the anode's gradual degradation over time. The electrolysis focused on the reduction processes and end products obtained from the regolith, rather than on the anodic processes. In real ISRU scenarios, an inert anode will be employed to produce oxygen directly and prevent carbon contamination.

In summary, future studies may need to further investigate the different phases formed during electrolysis, but this study has shown that it is possible to use Raman spectroscopy to detect changes in the samples related to the duration of electrolysis and therefore the amount of oxygen extracted.

4 Conclusion

The two separately presented studies show that LIBS and Raman spectroscopy are promising techniques to support ISRU activities. With LIBS we could show the suitability for the detection of enrichments of ilmenite and the potential for elemental

quantification. This was possible despite the fact that the used VOILA breadboard model was optimized for the detection of H and O and therefore not including the UV wavelength range where intense Ti and Fe emission can be detected, and furthermore with only limited sensitivity below 450 nm resulting there in noisy data. With an instrument optimized for the UV and lower visible spectral range even better results are expected. On the other hand, with Raman spectroscopy, we could show that a chemical alteration process can be monitored and changes in the sample can be seen. Here, however, the sample set was not ideal to demonstrate the potential of Raman spectroscopy for process surveillance since the metals and metaloxides forming from the lunar regolith simulant are weak Raman scatterers. In this particular use case, Raman spectroscopy seems most useful for the tracking of the primary raw material that enters the oxygen extraction process. Other use cases, where processes observing the extraction of hydrogen and water are monitored, could yield even better results with Raman spectroscopy. In another study (Vogt et al., 2022b), the same samples were measured with the VOILA LIBS setup and promising results for the monitoring of the LIBS O signal are reported. Thus, combining LIBS and Raman spectrocopy can result in a powerful approach for the *in-situ* characterisation of the lunar regolith and for the online monitoring of the extraction process.

Both studies share the conclusion that it is important to measure multiple positions per sample on the very fine grained and locally heterogeneous lunar regolith. At this point, it is relevant to note that the samples used in this study were prepared as pressed pellets with an even surface. Although geological samples may deviate from this, it should not be an issue if LIBS and Raman instruments have a focusing mechanism to ensure that each measuring point is in the optimal focus, regardless of the possible unevenness of samples. The anticipated sample heterogeneity has already been discussed for the LIBS study, which is why we recommend taking several measurements per sample. The acquisition of multiple measurements allows that statistical approaches can be included in the data analysis chain which are needed for more robust quantitative results. For LIBS we propose rasters with a minimum of 10 points and 20–50 shots per position to obtain also information from some depth. With LIBS, small craters of some mm depth can be obtained in the lunar regolith that could allow the detection of ice in the most shallow subsurface. For Raman analysis and a holistic assessment of the composition of samples, an even bigger raster is suggested in order to allow quantitative estimates from the distribution and number of detections of the measured minerals. In closing, both methods proved useful in their respective applied studies for ISRU applications, showing their potential to contribute to the efforts of achieving sustainable and scientifically fruitful lunar and eventually Martian missions.

Next steps would be the development of setups and breadboards dedicated to specific use cases in the framework of ISRU applications for more detailed investigations and feasibility studies, to include the analysis of space-related effects and to increase the technological readiness level (TRL) of prototypes.

Data availability statement

The raw data supporting the conclusion of this article will be made available by the authors upon request, without undue reservation.

Author contributions

KR: Conceptualization, Data curation, Formal Analysis, Investigation, Writing–original draft, Writing–review and editing, Methodology. SS: Conceptualization, Methodology, Supervision, Writing–original draft, Writing–review and editing. BL: Resources, Writing–review and editing, Methodology. EC: Methodology, Writing–review and editing, Conceptualization. H-WH: Funding acquisition, Writing–review and editing.

Funding

The author(s) declare financial support was received for the research, authorship, and/or publication of this article. This research was funded by DLR. Reduced simulant sample preparation was funded by ESA.

Acknowledgments

The authors would like to thank the Museum für Naturkunde Berlin for providing the ilmenite used for this study and Olivier Beyssac for fruitful discussions.

Conflict of interest

The authors declare that the research was conducted in the absence of any commercial or financial relationships that could be construed as a potential conflict of interest.

Publisher's note

Supplementary material

The Supplementary Material for this article can be found online at: https://www.frontiersin.org/articles/10.3389/frspt.2024.1336548/full#supplementary-material

References

Anand, M., Crawford, I. A., Balat-Pichelin, M., Abanades, S., Van Westrenen, W., Péraudeau, G., et al. (2012). A brief review of chemical and mineralogical resources on the Moon and likely initial *in situ* resource utilization (ISRU) applications. *Planet. Space Sci.* 74, 42–48. doi:10.1016/j.pss.2012.08.012

Andrews, D. G., Bonner, K., Butterworth, A., Calvert, H., Dagang, B., Dimond, K., et al. (2015). Defining a successful commercial asteroid mining program. *Acta Astronaut.* 108, 106–118. doi:10.1016/j.actaastro.2014.10.034

Baek, S.-J., Park, A., Ahn, Y.-J., and Choo, J. (2015). Baseline correction using asymmetrically reweighted penalized least squares smoothing. *Analyst* 140, 250–257. doi:10.1039/C4AN01061B

Bhartia, R., Beegle, L. W., DeFlores, L., Abbey, W., Razzell Hollis, J., Uckert, K., et al. (2021). Perseverance's scanning habitable environments with Raman and luminescence for organics and chemicals (SHERLOC) investigation. *Space Sci. Rev.* 217, 58. doi:10.1007/s11214-021-00812-z

Chen, G. Z., and Fray, D. J. (2020). "Invention and fundamentals of the FFC cambridge process," in *Extractive metallurgy of titanium* (Elsevier), 227–286. doi:10.1016/B978-0-12-817200-1.00011-9

Crawford, I., Anand, M., Cockell, C., Falcke, H., Green, D., Jaumann, R., et al. (2012). Back to the Moon: the scientific rationale for resuming lunar surface exploration. *Planet. Space Sci.* 74, 3–14. doi:10.1016/j.pss.2012.06.002

Crawford, I. A. (2015). Lunar resources: a review. *Prog. Phys. Geogr.* 39, 137–167. doi:10.1177/0309133314567585

Du, Y., Kou, M., Tu, J., Wang, M., and Jiao, S. (2021). An investigation into the anodic behavior of TiB2 in a CaCl2-based molten salt. *Corros. Sci.* 178, 109089. doi:10.1016/j.corsci.2020.109089

Dufresne, W. J., Rufledt, C. J., and Marshall, C. P. (2018). Raman spectroscopy of the eight natural carbonate minerals of calcite structure. *J. Raman Spectrosc.* 49, 1999–2007. doi:10.1002/jrs.5481

Effenberger, A. J., and Scott, J. R. (2010). Effect of atmospheric conditions on LIBS spectra. *Sensors* 10, 4907–4925. doi:10.3390/s100504907

Hagelschuer, T., Böttger, U., Buder, M., Bunduki, Y., Cho, Y., Dietz, E., et al. (2022). "Rax: the Raman spectrometer for the mmx phobos rover," in *73rd international astronautical congress*.

Harmon, R. S., Hark, R. R., Throckmorton, C. S., Rankey, E. C., Wise, M. A., Somers, A. M., et al. (2017). Geochemical fingerprinting by handheld laser-induced breakdown spectroscopy. *Geostand. Geoanalytical Res.* 41, 563–584. doi:10.1111/ggr.12175

Heiken, G., Vaniman, D., and French, B. M. (1991). *Lunar sourcebook: a user's guide to the Moon*, 1259. Cambridge University Press. Available at: https://www.lpi.usra.edu/publications/books/lunar_sourcebook/.

Hu, L., Song, Y., Ge, J., Jiao, S., and Cheng, J. (2016). Electrochemical metallurgy in $CaCl_2$-CaO melts on the basis of TiO_2·RuO_2Inert anode. *J. Electrochem. Soc.* 163, E33–E38. doi:10.1149/2.0131603jes

Islam, M. N., and Kumar, S. (2001). Influence of crystallite size distribution on the micro-Raman analysis of porous Si. *Appl. Phys. Lett.* 78, 715–717. doi:10.1063/1.1343494

Jehlička, J., and Culka, A. (2022). Critical evaluation of portable Raman spectrometers: from rock outcrops and planetary analogs to cultural heritage – a review. *Anal. Chim. Acta* 1209, 339027. doi:10.1016/j.aca.2021.339027

Kimura, Y., and Katoda, T. (1997). Effects of strain on crystallization of amorphous silicon characterized by laser Raman spectroscopy. *Appl. Surf. Sci.* 117-118, 790–793. doi:10.1016/S0169-4332(97)80184-5

Knight, A. K., Scherbarth, N. L., Cremers, D. A., and Ferris, M. J. (2000). Characterization of laser-induced breakdown spectroscopy (LIBS) for application to space exploration. *Appl. Spectrosc.* 54, 331–340. doi:10.1366/0003702001949591

Kubitza, S., Schröder, S., Dietz, E., Frohmann, S., Hansen, P. B., Rammelkamp, K., et al. (2020). Detecting sulfur on the Moon: the potential of vacuum ultraviolet laser-induced breakdown spectroscopy. *Spectrochim. Acta Part B At. Spectrosc.* 174, 105990. doi:10.1016/j.sab.2020.105990

Lasue, J., Wiens, R. C., Clegg, S. M., Vaniman, D. T., Joy, K. H., Humphries, S., et al. (2012). Remote laser-induced breakdown spectroscopy (LIBS) for lunar exploration. *J. Geophys. Res. E Planets* 117, 1–18. doi:10.1029/2011JE003898

Laxmiprasad, A. S., Sridhar Raja, V. L., Menon, S., Goswami, A., Rao, M. V., and Lohar, K. A. (2013). An *in situ* laser induced breakdown spectroscope (LIBS) for Chandrayaan-2 rover: ablation kinetics and emissivity estimations. *Adv. Space Res.* 52, 332–341. doi:10.1016/j.asr.2013.03.021

Lever, J., Krzywinski, M., and Altman, N. (2017). Principal component analysis. *Nat. Methods* 14, 641–642. doi:10.1038/nmeth.4346

Lomax, B. A., Conti, M., Khan, N., Bennett, N. S., Ganin, A. Y., and Symes, M. D. (2020). Proving the viability of an electrochemical process for the simultaneous extraction of oxygen and production of metal alloys from lunar regolith. *Planet. Space Sci.* 180, 104748. doi:10.1016/j.pss.2019.104748

Long-Fox, J. M., and Britt, D. T. (2023). Characterization of planetary regolith simulants for the research and development of space resource technologies. *Front. Space Technol.* 4, 1–16. doi:10.3389/frspt.2023.1255535

Losekamm, M. J., Biswas, J., Chupin, T., Deiml, M., Deremetz, M., Evagora, A. M., et al. (2022). Assessing the distribution of water ice and other volatiles at the lunar southsouth Pole with LUVMI-X: a mission concept. *Planet. Sci. J.* 3, 229. doi:10.3847/PSJ/ac8cfd

Lucey, P. G., Blewett, D. T., and Hawke, B. R. (1998). Mapping the FeO and TiO 2 content of the lunar surface with multispectral imagery. *J. Geophys. Res. Planets* 103, 3679–3699. doi:10.1029/97JE03019

Maurice, S., Clegg, S. M., Wiens, R. C., Gasnault, O., Rapin, W., Forni, O., et al. (2016). ChemCam activities and discoveries during the nominal mission of the mars science laboratory in Gale Crater, mars. *J. Anal. Atomic Spectrom.* 31, 863–889. doi:10.1039/c5ja00417a

Maurice, S., Wiens, R. C., Bernardi, P., Caïs, P., Robinson, S., Nelson, T., et al. (2021). The SuperCam instrument suite on the mars 2020 rover: science objectives and mast-unit description, 217. *Author*. doi:10.1007/s11214-021-00807-w

Maurice, S., Wiens, R. C., Saccoccio, M., Barraclough, B., Gasnault, O., Forni, O., et al. (2012). The ChemCam instrument suite on the Mars Science Laboratory (MSL) rover: science objectives and mast unit description. *Space Sci. Rev.* 170, 95–166. doi:10.1007/s11214-012-9912-2

McKay, D. S., Heiken, G., Basu, A., Blanford, G., Simon, S., Reedy, R., et al. (1991). "The lunar regolith," in *Lunar sourcebook, A user's guide to the moon*. Editors G. H. Heiken, D. T. Vaniman, and B. M. French, 285–356.

Meurisse, A., Lomax, B., Selmeci, Á., Conti, M., Lindner, R., Makaya, A., et al. (2022). Lower temperature electrochemical reduction of lunar regolith simulants in molten salts. *Planet. Space Sci.* 211, 105408. doi:10.1016/j.pss.2021.105408

Michel, P., Ulamec, S., Böttger, U., Grott, M., Murdoch, N., Vernazza, P., et al. (2022). The MMX rover: performing *in situ* surface investigations on Phobos. *Earth, Planets Space* 74, 2. doi:10.1186/s40623-021-01464-7

Müller, S., Meima, J. A., and Rammlmair, D. (2021). Detecting REE-rich areas in heterogeneous drill cores from Storkwitz using LIBS and a combination of k-means clustering and spatial raster analysis. *J. Geochem. Explor.* 221, 106697. doi:10.1016/j.gexplo.2020.106697

Noll, R., Fricke-Begemann, C., Brunk, M., Connemann, S., Meinhardt, C., Scharun, M., et al. (2014). Laser-induced breakdown spectroscopy expands into industrial applications. *Spectrochim. Acta Part B At. Spectrosc.* 93, 41–51. doi:10.1016/j.sab.2014.02.001

Pauca, V. P., Piper, J., and Plemmons, R. J. (2006). Nonnegative matrix factorization for spectral data analysis. *Linear Algebra its Appl.* 416, 29–47. doi:10.1016/j.laa.2005.06.025

Pedarnig, J. D., Trautner, S., Grünberger, S., Giannakaris, N., Eschlböck-Fuchs, S., and Hofstadler, J. (2021). Review of element analysis of industrial materials by in-line laser—induced breakdown spectroscopy (LIBS). *Appl. Sci.* 11, 9274. doi:10.3390/app11199274

Pořízka, P., Klus, J., Képeš, E., Prochazka, D., Hahn, D. W., and Kaiser, J. (2018). On the utilization of principal component analysis in laser-induced breakdown spectroscopy data analysis, a review. *Spectrochim. Acta Part B At. Spectrosc.* 148, 65–82. doi:10.1016/j.sab.2018.05.030

Rammelkamp, K., Schröder, S., Ortenzi, G., Pisello, A., Stephan, K., Baqué, M., et al. (2021). Field investigation of volcanic deposits on Vulcano, Italy using a handheld laser-induced breakdown spectroscopy instrument. *Spectrochim. Acta - Part B At. Spectrosc.* 177, 106067. doi:10.1016/j.sab.2021.106067

Rapin, W., Maurice, S., Ollila, A., Wiens, R. C., Dubois, B., Nelson, T., et al. (2023). "μlibs: a micro-scale elemenal analyser for lightweight *in situ* exploration," in *54th lunar and planetary science conference* (Houston: Lunar and Planetary Institute). Abstract #1942.

Reich, S., and Thomsen, C. (2004). Raman spectroscopy of graphite. *Philosophical Trans. R. Soc. Lond. Ser. A Math. Phys. Eng. Sci.* 362, 2271–2288. doi:10.1098/rsta.2004.1454

Rull, F., Maurice, S., Hutchinson, I., Moral, A., Perez, C., Diaz, C., et al. (2017). The Raman laser spectrometer for the ExoMars rover mission to mars. *Astrobiology* 17, 627–654. doi:10.1089/ast.2016.1567

Schlüter, L., and Cowley, A. (2020). Review of techniques for *In-Situ* oxygen extraction on the moon. *Planet. Space Sci.* 181, 104753. doi:10.1016/j.pss.2019.104753

Schröder, S., Böttger, U., Buder, M., Bunduki, Y., Cho, Y., Dietz, E., et al. (2023). "Rax: the Raman spectrometer on the mmx rover for *in-situ* surface analysis on phobos," in *54th lunar and planetary science conference* (Houston: Lunar and Planetary Institute). Abstract #2549.

Senesi, G. S. (2014). Laser-Induced Breakdown Spectroscopy (LIBS) applied to terrestrial and extraterrestrial analogue geomaterials with emphasis to minerals and rocks. *Earth-Science Rev.* 139, 231–267. doi:10.1016/j.earscirev.2014.09.008

Senesi, G. S., Harmon, R. S., and Hark, R. R. (2021). Field-portable and handheld laser-induced breakdown spectroscopy: historical review, current status and future prospects. *Spectrochim. Acta - Part B At. Spectrosc.* 175, 106013. doi:10.1016/j.sab.2020.106013

Stephan, K., Hibbitts, C., Hoffmann, H., and Jaumann, R. (2008). Reduction of instrument-dependent noise in hyperspectral image data using the principal component analysis: applications to galileo nims data. *Planet. Space Sci.* 56, 406–419. doi:10.1016/j.pss.2007.11.021

Strubbe, D. A., Johlin, E. C., Kirkpatrick, T. R., Buonassisi, T., and Grossman, J. C. (2015). Stress effects on the Raman spectrum of an amorphous material: theory and experiment on a-Si:H. *Phys. Rev. B* 92, 241202. doi:10.1103/PhysRevB.92.241202

Ulamec, S., Michel, P., Grott, M., Böttger, U., Schröder, S., Hübers, H. W., et al. (2023). Science objectives of the MMX rover. *Acta Astronaut.* 210, 95–101. doi:10.1016/j.actaastro.2023.05.012

Ureña, F., Olsen, S. H., and Raskin, J.-P. (2013). Raman measurements of uniaxial strain in silicon nanostructures. *J. Appl. Phys.* 114. doi:10.1063/1.4824291

Vogt, D. S., Schröder, S., Richter, L., Deiml, M., Weßels, P., Neumann, J., et al. (2022a). VOILA on the LUVMI-X rover: laser-induced breakdown spectroscopy for the detection of volatiles at the lunar southsouth Pole. *Sensors* 22, 9518. doi:10.3390/s22239518

Vogt, D. S., Schröder, S., Sandig, N., Gensch, M., Hübers, H.-W., Lomax, B., et al. (2022b). "Laser-induced breakdown spectroscopy for the support of *in-situ* resource utilization (isru) on the moon," in *53rd lunar and planetary science conference* (Houston: Lunar and Planetary Institute). Abstract #1872.

Wan, X., Li, C., Wang, H., Xu, W., Jia, J., Xin, Y., et al. (2021). Design, function, and implementation of China's first libs instrument (Marscode) on the zhurong mars rover. *At. Spectrosc.* 42, 294–298. doi:10.46770/AS.2021.608

Wiens, R. C., Maurice, S., Barraclough, B., Saccoccio, M., Barkley, W. C., Bell, J. F., et al. (2012). The ChemCam instrument suite on the Mars Science Laboratory (MSL) rover: body unit and combined system tests. *Space Sci. Rev.* 170, 167–227. doi:10.1007/s11214-012-9902-4

Wiens, R. C., Maurice, S., Robinson, S. H., Nelson, A. E., Cais, P., Bernardi, P., et al. (2021). *The SuperCam instrument suite on the NASA Mars 2020 rover: body unit and combined system tests*, 217. Space Science Reviews. Available at: https://link.springer.com/article/10.1007/s11214-020-00777-5.

Xu, W., Liu, X., Yan, Z., Li, L., Zhang, Z., Kuang, Y., et al. (2021). *The MarSCoDe instrument suite on the Mars rover of China's tianwen-1 mission*, 217. Springer Nature B.V. The Author(s), under exclusive licence to. doi:10.1007/s11214-021-00836-5

Zwick, A., and Carles, R. (1993). Multiple-order Raman scattering in crystalline and amorphous silicon. *Phys. Rev. B* 48, 6024–6032. doi:10.1103/PhysRevB.48.6024